

1 A refined characterization of large-scale genomic differences 2 in the first complete human genome

3
4 Xiangyu Yang^{1,†}, Xuankai Wang^{1,†}, Yawen Zou¹, Shilong Zhang¹, Manying Xia¹, Mitchell R.
5 Vollger², Nae-Chyun Chen³, Dylan J. Taylor⁴, William T. Harvey², Glennis A. Logsdon²,
6 Dan Meng¹, Junfeng Shi^{5,6}, Rajiv C. McCoy⁴, Michael C. Schatz^{3,4}, Weidong Li¹, Evan E.
7 Eichler^{2,7}, Qing Lu¹, Yafei Mao^{1,6,*}

8
9 ¹*Bio-X Institutes, Key Laboratory for the Genetics of Developmental and Neuropsychiatric*
10 *Disorders, Ministry of Education, Shanghai Jiao Tong University, Shanghai, China.*

11 ²*Department of Genome Sciences, University of Washington School of Medicine, Seattle,*
12 *WA, USA.*

13 ³*Department of Computer Science, Johns Hopkins University, Baltimore, MD, USA.*

14 ⁴*Department of Biology, Johns Hopkins University, Baltimore, MD, USA.*

15 ⁵*Shanghai Engineering Research Center of Advanced Dental Technology and Materials,*
16 *Shanghai, China.*

17 ⁶*Shanghai Key Laboratory of Stomatology, Shanghai Ninth People's Hospital, College of*
18 *Stomatology, Shanghai Jiao Tong University School of Medicine, Shanghai, China.*

19 ⁷*Howard Hughes Medical Institute, University of Washington, Seattle, WA, USA.*

20 [†]: These authors contributed equally: Xiangyu Yang, Xuankai Wang

21 *Corresponding author: yafmao@sjtu.edu.cn

22 **Abstract**

23 The first telomere-to-telomere (T2T) human genome assembly (T2T-CHM13) release was a
24 milestone in human genomics. The T2T-CHM13 genome assembly extends our
25 understanding of telomeres, centromeres, segmental duplication, and other complex regions.
26 The current human genome reference (GRCh38) has been widely used in various human
27 genomic studies. However, the large-scale genomic differences between these two important
28 genome assemblies are not characterized in detail yet. Here, we identify 590 discrepant
29 regions (~226 Mbp) in total. In addition to the previously reported ‘non-syntenic’ regions, we
30 identify 67 additional large-scale discrepant regions and precisely categorize them into four
31 structural types with a newly developed website tool (SynPlotter). The discrepant regions
32 (~20.4 Mbp) excluding telomeric and centromeric regions are highly structurally
33 polymorphic in humans, where copy number variation are likely associated with various
34 human disease and disease susceptibility, such as immune and neurodevelopmental disorders.
35 The analyses of a newly identified discrepant region—the *KLRC* gene cluster—shows that
36 the depletion of *KLRC2* by a single deletion event is associated with natural killer cell
37 differentiation in ~20% of humans. Meanwhile, the rapid amino acid replacements within
38 *KLRC3* is consistent with the action of natural selection during primate evolution. Our study
39 furthers our understanding of the large-scale structural variation differences between these
40 two crucial human reference genomes and future interpretation of studies of human genetic
41 variation.

42 **Introduction**

43 The first draft human genome published two decades ago has contributed enormously to
44 human genomics, medical genomics, evolutionary genomics, and other fields^{1,2}. Given efforts
45 to refine and construct the sequence from Genome Reference Consortium, the current human
46 reference genome assembly (GRCh38) has been widely used for understanding human
47 diversity, disease-related variants, and human/primate evolution³. The GRCh38 genome
48 assembly has been annotated with abundant resources including gene annotation, gene
49 expression, gene regulation, and others³. Despite the high quality of the GRCh38 reference, it
50 still has hundreds of gaps and errors in GRCh38⁴. These gaps and errors represented long-
51 standing obstacles to fully understanding human genomics, especially in repetitive regions⁴⁻¹⁰
52. With advances in long-read sequencing and computational algorithms, the Telomere to
53 Telomere (T2T) Consortium has finally achieved the goal of building a gapless and accurate
54 assembly of a human genome⁴⁻⁹.

55

56 The release of the complete genome (T2T-CHM13) provides the first complete sequence
57 view of centromeres, telomeres, tandem repeat arrays, segmental duplications (segdups), and
58 the p-arms of acrocentric chromosomes in the human genome⁴⁻¹¹. As a result, the T2T
59 Consortium also provided insights into the organization and function of segdups,
60 centromeres, epigenetic features of repeats and genome, and human genetic variation by
61 comparative genomics and population genetics approaches⁴⁻⁹. These efforts significantly
62 extend our biological understanding of human genomics and underscore the advantages of
63 using T2T-CHM13 as a reference for genomic analyses¹¹.

64

65 More than 200 Mbp of genomic sequences were identified as ‘non-syntenic’ regions between
66 GRCh38 and T2T-CHM13 in the previous studies^{4,9}, representing major of large-scale
67 genomic differences between these two assemblies. The large-scale genomic differences are
68 largely concentrated in complex genomic regions, which play an outstanding role in human
69 disease as well as evolutionary adaptation^{10,12}. For example, segdups of *Notch2NL* are
70 associated with brain development in primate evolution, while a rare microdeletion of
71 *Notch2NL* causes microcephaly in humans¹³⁻¹⁶. We sought to revisit this analysis using
72 different methods in order to further refine and assess the large-scale genomic differences
73 between GRCh38 and T2T-CHM13 for future applications (e.g., genotyping, association, and
74 evolutionary studies).

75

76 Here, we expand on the comparison of ‘non-syntenic’ regions between T2T-CHM13 and
77 GRCh38 in the previous studies^{4,9}, identifying additional large-scale genomic differences
78 between these two assemblies applying an array of additional alignment and visual validation
79 tools. We characterize the genomic regions with at least 10 kbp genomic differences between
80 the two assemblies into four types: insertions, deletions, inversions, and structural divergent
81 regions (SDRs), with respect to GRCh38. We then develop an integrated website tool
82 (SynPlotter, <https://synplotter.sjtu.edu.cn/>) to validate the discrepant regions and characterize
83 the gene model differences in these regions. In addition, we use the 239 human genomes
84 from the Simons Genome Diversity Project (SGDP)¹⁷ to test whether these discrepant regions
85 are likely copy number (CN) polymorphic in human populations. We also investigate the
86 functional relationship between discrepant regions and human diseases. Finally, we
87 systematically analyze the evolutionary history of one example of a newly identified
88 discrepant region—the *KLRC* gene cluster—in human populations and other nonhuman
89 primates.

90

91 **Results**

92 ***Large-scale genomic discrepant regions***

93 More than 570 ‘non-syntenic’ regions (~238Mbp) have been identified between the T2T-
94 CHM13 and GRCh38 genome assembly with a 1Mbp syntenic interval approach^{4,9}. Here, to
95 more completely and precisely characterize the structural types of the large-scale genomic
96 differences between the two genome assemblies, we applied three additional alignment tools
97 (PAV^{18,19}, minigraph²⁰, PBSV (<https://github.com/PacificBiosciences/pbsv>)) to expand on the
98 non-syntenic regions originally identified by LASTZ^{4,9}. We identified the 695 structural
99 variants (SVs, ≥ 10 kbp) with three independent methods (Tables S1-S3). Next, we developed
100 an integrated website tool (SynPlotter) that is designed to visualize and cross-validate the
101 syntenic relationship between GRCh38 and T2T-CHM13 by integrating multiple aligners
102 (e.g., minimap2 and numer) and publicly available visualization tools (e.g., dotplot and
103 Saffire (unpublished, <https://mr vollger.github.io/Saffire>))^{21,22}. Excluding the SVs in
104 centromere and telomere regions, we validated 238 of 274 large SVs (validation rate: 86.9%)
105 using our validation tool (Table S4).

106

107 Next, we integrated our validated large SVs with the validated ‘non-syntenic’ regions (Fig.
108 1a, Fig. S1, and Table S4) for a total of 590 discrepant genomic regions (~226 Mbp) between
109 GRCh38 and T2T-CHM13 in total (Fig. 1b). Of these, 295 regions are in centromeres

110 (204.64 Mbp), 57 regions are in (sub)telomeres (1.23 Mbp), 162 regions are in segdups
111 (17.86 Mbp), 18 regions are in tandem repeats (0.56 Mbp), while 58 regions occur in other
112 parts of the genome (1.98 Mbp) (Fig. 1b).

113

114 We excluded 352 discrepant regions in centromeres and telomeres and focused on the
115 euchromatic regions^{4-9,23}. We refined the characterization of the large-scale discrepant
116 regions by categorizing them into four types (including: insertions, deletions, inversions, and
117 SDRs, with respect to GRCh38) with more precise breakpoints (Fig. 1c). There are 23
118 deletions (1.51 Mbp), 83 insertions (3.42 Mbp), 39 inversions (10.47 Mbp) and 26 SDRs
119 (1.87 Mbp) in the previously reported ‘non-syntenic’ regions (total: 17.27 Mbp) (Fig. 1c).
120 Relative to the previously reported ‘non-syntenic’ regions, here, we found 67 newly
121 identified discrepant regions, of which the number is ~40% greater than that of the reported
122 ‘non-syntenic’ regions (Fig. 1c). The 67 newly identified regions (total: 3.13 Mbp) include 45
123 deletions (1.7 Mbp), 4 insertions (0.06 Mbp), and 18 inversions (1.37 Mbp) (Fig. 1c). The
124 number of deletions in the newly identified set is higher than in the ‘non-syntenic’ regions (p
125 <0.001, chi-square test).

126

127 ***Gene model and structure differences in the CN polymorphic discrepant regions***

128 Of the 238 discrepant regions, 63 of them include 153 genes, such as *TBC1D3*, *AMY1*,
129 *GPRIN2*, and *NOTCH2NL* (reported in the ‘non-syntenic’ regions)^{4,9}. Of these, 53 protein-
130 coding genes are in the 25 newly-identified discrepant regions, including *ZDHCC11B*,
131 *GSTM2*, *CFHR3*, *CFHR1*, *CR1*, and *KLRC2* (Table S5). The depletion of *ZDHHC11B* is found
132 in T2T-CHM13 by a ~98 kbp deletion, with respect to GRCh38 (Fig. 2a). The read-depth
133 genotyping from 206 Illumina short read genomes from the SGPD shows the CN
134 polymorphism of *ZDHHC11* in humans (Fig. 2a). The gene models showed that the two
135 exons are deleted in *ZDHHC11B* compared to *ZDHHC11* (Fig. 2a). We also observed the
136 depletion of *GSTM1* in T2T-CHM13 by a ~17 kbp deletion and the *GSTM* is inferred as CN
137 polymorphic in the 206 humans (Fig. 2b). The gene models showed that a few amino acids of
138 *GSTM1* are different from that of *GSTM2* (Fig. 2b). In addition, we observed an ~18.5 kbp
139 deletion in T2T-CHM13, resulting in the depletion of eight exons (450 amino acids) in *CR1*
140 (Fig. 2c). We examined the length of *CR1* gene in the 94 long-read human genome assembly
141 from the Human PanGenome Reference Consortium (HPRC)²⁴⁻²⁶ and the length of *CR1* in 79
142 assemblies coincides with that of T2T-CHM13. This suggests that T2T-CHM13 carries the
143 major allele of *CR1* (allele frequency: 0.84) (Fig. S2). In addition, another ~85 kbp genomic

144 region, including *CFHR1* and *CFHR3*, is deleted in T2T-CHM13, with respect to GRCh38
145 (Fig. S3).

146

147 We assessed whether the discrepant regions are likely CN polymorphic in the human
148 genome. We used the standard deviation (s.d.) of the CN as an index to represent the level of
149 polymorphisms (see Methods)²⁷. To reduce the CN estimation bias, we excluded the regions
150 where the CN is greater than 10 in the following analyses. We observed that the mean s.d.
151 of the CN of the 131 discrepant regions (mean=0.67) is ~5-fold greater than that of the whole
152 genomic regions (mean=0.13, empirical p=0) (Fig. 2d and Fig. S4), as expected. We next
153 tested whether the discrepant regions are more likely CN polymorphic than the CN variable
154 regions (CN>2.5 and CN<10). We observed the mean s.d. of the CN of the 131 discrepant
155 regions (mean=0.58) is ~1.2-fold greater than that of the CN variable regions (mean=0.58,
156 empirical p=0.003) (Fig. 2e). Yet, we did not observe a significant difference between the
157 median s.d. of the CN of the 131 discrepant regions (median=0.46) and that of the CN
158 variable genomic regions (median=0.4, empirical p=0.07) (Fig. S4). The simulation tests
159 imply that the discrepant regions are more likely CN polymorphic than the genome-wide
160 average, maybe even than the CN variable regions in the human genome. These results
161 suggest that the gene structure/model differences in the CN polymorphic discrepant regions
162 warrant further investigation for potential disease association and functional assessment.

163

164 ***Disease relevant loci are associated with the large-scale discrepant regions***

165 We integrated the reported morbid copy number variants (CNVs) and genomic disorder
166 CNVs that associated with more than 50 disease phenotypes, including neurodevelopmental
167 disorders, abnormality of the immune system, and others²⁸⁻³⁰. We next queried whether the
168 discrepant regions are more likely associated with the reported disease relevant CNVs. With
169 genome-wide permutation analysis (see Methods), we found that the discrepant regions are
170 significantly co-localized with disease relevant CNVs (empirical p=0.003, ~1.7-fold excess)
171 (Fig. S5). To better characterize the genes/genomic coordinates relevant to disease, we
172 surveyed the literature and DECIPHER database for the aforementioned discrepant regions
173 and found 27 discrepant regions associated with human diseases; 18 of them are newly
174 identified discrepant regions (Table 1).

175

176 The genes in the 27 disease relevant discrepant regions are enriched in the neuroblastoma
177 breakpoint family domain ($p=3.9e-5$), complement and coagulation cascades ($p=7.5e-4$),
178 glutathione metabolic process ($p=4.4e-3$), and antimicrobial ($p=5.5e-5$) by the gene ontology
179 (GO) enrichment analysis (Table S6). Therefore, the rare microdeletions or microduplications
180 of these discrepant regions mainly affect the development and function of the circulatory
181 system (urinary system disease (e.g., chromosome 1p13.3)), immune system (COVID-19
182 (e.g., 6p21.32, 12p13.2)), and nervous system (bipolar disorder/schizophrenia³¹(e.g.,
183 10q11.22) and autism spectrum disorder (e.g., 16p12)) (Table 1). We also found some genes
184 within the discrepant regions that are proven to be functionally well-known and pathogenic.
185 For example, *KLRC2*, located in a newly identified discrepant regions, is involved in immune
186 cell maturation and subtype differentiation³². The *KLRC2* protein (also: NKG2C) can bind to
187 CD94 and HLA-E to form a functional complex³³, and thus, the depletion of *KLRC2* is likely
188 to have a significant impact on the development of severe COVID-19³⁴. In the visual cortex,
189 microglial CD94/ *KLRC2* is necessary for regulating the magnitude of ocular dominance
190 plasticity during the critical period of development³⁵. *GSTM1* (Glutathione S-Transferase Mu
191 1) encodes a member of a superfamily of antioxidant enzymes, which is important in kidney
192 disease progression³⁶. *ZDHHC11B* (Zinc Finger DHHC-Type Containing 11B) is involved in
193 a network that promotes the proliferation of Burkitt lymphoma cells³⁷. *CFHR3* and *CFHR1*,
194 belonging to Complement factor H (CFH), plays an essential role in regulating the alternative
195 pathway of the complement system³⁸. These results suggest that the discrepant genomic
196 regions are functionally important and need to be considered carefully with respect to
197 genome-wide association.

198

199 ***The diversity of KLRC2 characterized with the 94 long-read and 2,504 short-read human
200 genomes***

201 We observed that *KLRC2* is deleted by a 15.4 kbp deletion variant in T2T-CHM13, with
202 respect to GRCh38 (Fig. 3a). This discrepant region is CN polymorphic in human
203 populations as evidenced by SGPD read-depth genotyping³⁹⁻⁴¹ (Fig. S6). To better
204 characterize the diversity of the *KLRC* region, we systematically investigated the discrepant
205 region with the 94 long-read genome assemblies from the HPRC dataset²⁴⁻²⁶. We found 1
206 duplication and 11 deletions of *KLRC2* in the 94 long-read genome assemblies (Table S7).
207 We refined the breakpoints of the duplication and deletion of *KLRC2* in the T2T-CHM13 and
208 HG002_hap¹⁹ genome assemblies at single-base pair resolution to understand the
209 mechanisms of the structural variation.

210
211 There are four *KLRC* genes in the *KLRC* discrepant region, wherein a segdup including
212 *KLRC2* and *KLRC3* represents is configured in a direct orientation⁴² (Fig. 3). The
213 configuration provides a genetic basis for microdeletions and microduplications of *KLRC2*.
214 The syntenic relationship of the *KLRC* gene cluster between T2T-CHM13 and GRCh38
215 revealed that the left breakpoint of the *KLRC2* deletion is located within *AluYm1*, and the
216 right breakpoint of the *KLRC2* deletion is 3 bp away from another *AluYm1* (Fig. 3b). We
217 also observed a 43 bp repeat motif (tgatgcctccaaagtgcgtggattataggcttgagccacca) at both
218 breakpoints (Fig. 3b). In addition, we refined the breakpoints of the *KLRC2* duplication in the
219 HG002_hap1 assembly (Fig. 3c). We found that the duplication sequences (~15.4 kbp) are
220 inserted in an *AluJb* element and the *AluJb* element is disrupted by a simple repeat insertion
221 in GRCh38 (Fig. 3d). The breakpoints are located within ploy adenine (polyA) sequences in
222 GRCh38 (Fig. 3d).
223
224 Our analysis of the long-read HPRC haplotypes (n=94) identified three haplotypes of the
225 *KLRC* gene cluster, including 0, 1, and 2 copies of *KLRC2*, respectively. Next, we used the
226 SUNK (singly unique nucleotide *k*-mer) mapping and read-depth genotyping approaches³⁹⁻⁴¹
227 to infer the three haplotypes in 2,504 human genomes from the 1,000 Genome Project
228 (1KG)⁴³. We found that 19%, 78%, and 3% of modern humans contain 0, 1, and 2 copies of
229 *KLRC2*, respectively (Fig. 4a, Table S8). The haplotype with a depleted *KLRC2* (“*KLRC-*
230 *hap2*”) occurs more frequently in African (e.g., Esans: 25.45%) and East Asian (e.g., Kinhs:
231 26.24%) populations but is observed less frequently in American (e.g., Peruvians: 3.8%) and
232 South Asian (e.g., Pakistans: 9.71%) populations (Table S9).
233
234 To study whether the depletion of *KLRC2* is a recurrent or a single-deletion event in human
235 populations, we used the ~12.7 kbp *KLRC* gene cluster genomic regions, including both
236 *KLRC2* and *KLRC3*, to reconstruct the phylogenetic tree of the 94 long-read human samples.
237 The results showed that the *KLRC2* depletion haplotypes from different human groups are
238 monophyletic (Fig. 4b), suggesting that the *KLRC*-*hap2* (*KLRC2* depletion) deletion arose
239 once in human population history.
240
241 ***Gene expression and NK cell differentiation between two KLRC haplotypes***
242 To investigate potential functional effects of different *KLRC2* haplotypes in humans, we
243 identified six single-nucleotide variants (SNVs) that distinguish *KLRC*-*hap2* (*KLRC2*

244 depletion) from *KLRC*-hap1 (one copy *KLRC2*) with the 94 long-read genome assemblies.
245 We examined the linkage disequilibrium (LD) of the *KLRC* gene cluster among 2,504 high-
246 coverage genomes from the 1KG human population. In general, the *KLRC* gene cluster shows
247 significant LD (LD: $r^2 > 0.5$, D' > 0.5) (Fig. 4c). In particular, the six SNVs identified in the 94
248 long-read genome assemblies are tightly linked (LD: $r^2 > 0.9$; D' > 0.99) (Fig. 4c). These six
249 SNVs can, thus, be used to infer the deletion haplotype. Indeed, we find that the allele
250 frequencies of the six SNVs of the *KLRC*-hap2 in ~135,000 humans from the gnomAD
251 database are from 19.9% to 20.6%, which coincide with the CN frequency of *KLRC*-hap2 in
252 humans from our above *KLRC*-haplotype inference analysis (Fig. 4c and Table S10).

253

254 Of note, the six SNVs are identical between GRCh38 and T2T-CHM13, although apparently
255 distinguish two distinct *KLRC* haplotypes (GRCh38: *KLRC*-hap1, T2T-CHM13: *KLRC*-
256 hap2). We investigated whether this apparent discrepancy could have resulted from a ‘mixed’
257 haplotype in GRCh38. In GRCh38, we note that the region was assembled by the two distinct
258 bacterial artificial chromosome (BAC) clones (AC022075.29 and AC068775.52) from one
259 donor (RP11) (Fig. 4c). Previous studies have shown that haplotype swaps are usually
260 associated with the overlap boundary of the two adjacent BAC clones⁶. In support of this, our
261 LD analysis within the *KLRC* locus (see Methods), shows that GRCh38 possesses
262 combinations of alleles that are either in strong positive or strong negative LD, whereas the
263 corresponding region of T2T-CHM13 largely exhibits alleles only in positive LD. Thus, T2T-
264 CHM13 better reflects the haplotype structure of living human populations. LD at the *KLRC*
265 locus extends much further than the randomly selected control locus, which exhibits multiple,
266 shorter haplotype blocks, potentially reflecting differences in the history of recombination
267 within the regions or a deep coalescent deletion (Fig. S7 and Fig. S8). Taken together, we
268 consider the *KLRC* gene cluster organization in GRCh38 to represent the product of a
269 misassembly of two different haplotypes.

270

271 Using the GTEx (Genotype-Tissue Expression) multi-tissue eQTL (expression quantitative
272 trait loci) database (release v8, <https://gtexportal.org/>), we investigated how these six SNVs
273 relate to *KLRC2* gene expression differences among 54 different tissues. We show that
274 *KLRC*-hap2 SNVs correspond to reduced expression of *KLRC2* gene in 35 tissues (Fig. 4d).
275 In particular, the brain and spleen tissues show the most significant gene expression
276 difference between two haplotypes ($p < 2e-5$). Further, we investigated the association

277 between these six SNVs with more than 600 phenotypes/traits (GWAS Atlas) and find that
278 three out of six SNVs are significantly associated with immune domain function involving in
279 the NK cell differentiation ($p < 1e-15$)^{32,44} (Fig. 4e). These results suggest that the depletion of
280 *KLRC2* likely plays a role in the immune differentiation.

281

282 ***The evolutionary history of KLRC2 and KLRC3 in primates***

283 Using sequence read-depth, we investigated CN of *KLRC* genes among a population of non-
284 human primates (NHPs). Our analysis revealed that *KLRC2* and *KLRC3* are also CN
285 polymorphic and that *KLRC2* and *KLRC3* CN in the African great apes is greater than other
286 primates (Fig. S9). We also investigated the organization of the *KLRC* gene cluster within 16
287 long-read genome assemblies. The analysis confirmed *KLRC2* and *KLRC3* are CNV in NHPs
288 with a deletion of *KLRC2* and *KLRC3* in two gibbon genome assemblies (Fig. S10) and three
289 copies of *KLRC2* in two macaque genome assemblies (Fig. S11). We reconstructed the
290 phylogenetic tree of *KLRC2* and *KLRC3* using ~5.5 kbp genomic region. The phylogenetic tree
291 shows that *KLRC2* and *KLRC3* were duplicated within the common ancestor of apes and Old
292 World monkey at ~19.8 million years ago (mya) (95% CI: 10.85-28.97 mya) (Fig. 5a and
293 Fig. S12). In addition, we found that *KLRC2* is independently duplicated in humans and
294 macaques (Fig. 5a).

295

296 We also examined *KLRC2* and *KLRC3* duplicated genes for evidence of natural selection
297 during primate evolution. An analysis of diversity of the *KLRC* gene cluster based on the 94
298 long-read genome assemblies revealed no significant differences based on pi diversity
299 estimates (Fig. S13). In contrast, a branch model estimate of amino acid selection, as defined
300 by PAML and aBSREL (an adaptive branch-site REL test for episodic diversification), found
301 evidence of selection within the *KLRC3* clade ($p=0.03$, likelihood ratio test)^{45,46} (Table S11).
302 In particular, we identified three amino acids (R224, R227, G229) of *KLRC3* predicted to be
303 under positive selection with greater 90% possibility by the branch-site model implemented
304 in PAML ($p=0.006$, likelihood ratio test) (Fig. 5b and Table S11).

305

306 Based on the AlphaFold2 and *KLRC1* crystal structure^{33,47}, the protein structure of *KLRC2*
307 and *KLRC3* are predicted to be altered by these three amino acids (Fig. 5b). *KLRC* proteins
308 have been shown to bind CD94 and HLA-E for immune response^{33,47}. With predicted
309 complex protein structure of *KLRC*/HLA-E/CD94, significant differences were found
310 between the interaction interfaces of *KLRC2*/HLA-E and *KLRC3*/HLA-E. Two hydrogen

311 bonds were observed between the C-terminal of KLRC3 and HLA-E: the amide nitrogen of
312 Ile226 from KLRC3 binds the side chain of Glu175 from HLA-E; the side chain Arg227
313 from KLRC3 binds the carbonyl oxygen of Asp170 from HLA-E. The two hydrogen bonds
314 may stabilize the flexible loop of KLRC3 (Fig. 5c). However, no obvious interactions were
315 found between the C-terminal of KLRC2 and HLA-E (Fig. 5c). Our findings implicate
316 differential binding affinity at the two interaction interfaces potentially important for
317 functional differentiation of KLRC2 and KLRC3 in humans.

318

319 **Discussion**

320 The first complete genome assembly (T2T-CHM13) represents a new and important
321 genomics resource^{4-11,48,49}. Here, we more systematically investigate the large-scale genomic
322 differences between T2T-CHM13 and the current reference genome assembly (GRCh38). We
323 show that the discrepant regions are among the most structurally complex and may introduce
324 reference biases in human genetics (e.g., genotype-phenotype association study) and
325 evolutionary genomics (e.g., gene family evolution investigation). Therefore, understanding
326 the discrepant regions between the two crucial reference genome assemblies will provide a
327 crucial resource for further genomic and functional studies. In this study, we systematically
328 characterized the large SVs between the two human genome assemblies and found 67 newly
329 identified discrepant regions. In addition, we developed an integrated website tool
330 (SynPlotter) to visualize and validate 246 discrepant regions. The newly identified regions
331 include gene-model differences (e.g., *ZDCHH1B*, *GSTM1*, *CFHR3*, *CFHR1*, *CR1*, and
332 *KLRC2*) and the SGDP read-depth genotyping data show that the discrepant regions are more
333 likely CN polymorphic. In addition, the discrepant regions are often related to human
334 diseases. Finally, we provided a novel example to illustrate the biological importance of
335 discrepant regions by analyzing the *KLRC* gene cluster with population genetics and
336 evolutionary genomic approaches.

337

338 Previous studies used a 1Mbp syntenic intervals to identify the sequence difference between
339 the two genome assemblies^{4,9}. Here, we used three different methods to identify the SVs (≥ 10
340 kbp) with reciprocal alignment between GRCh38 and T2T-CHM13 to identify precise
341 breakpoints and structural types of the large-scale discrepant regions (Fig. S1). We
342 additionally identified the 67 discrepant regions and ~70% of them belongs to deletions,
343 because deletion variants are likely chained in a large synteny by the LASTZ^{4,9}. Notably,
344 comparing with the recent inversion dataset in humans⁵⁰, we found that one inversion in our

345 dataset was not reported in the dataset⁵⁰. The genomic region of the inversion contains a gap
346 in GRCh38 (Fig. S14). This shows the SV discovery would be affected by the reference bias
347 and T2T-CHM13 is useful to identify large-scale SVs. In addition, we developed an
348 integrated visualization tool to validate the discrepant regions. This website tool is user-
349 friendly and publicly available to compare syntenic regions between GRCh38 and T2T-
350 CHM13.

351

352 The discrepant regions between these two assemblies have been regarded as CN polymorphic
353 genomic regions in previous studies^{4,6,9}. We performed CN analysis to provide clear evidence
354 to support that the discrepant regions are likely more polymorphic than the genome-wide
355 average, even than the CN variable regions. In addition, to our knowledge, we surveyed the
356 relevance between the discrepant regions and the reported medical relevant loci in greater
357 detail. We find that rare microdeletions and microduplications of 27 discrepant regions are
358 potentially related to neurodevelopmental diseases and others with supported evidence²⁸⁻³⁰.
359 Loss of function of *CR1* is associated with the Alzheimer's disease^{51,52} and T2T-CHM13
360 carries a major allele of *CR1*. Yet, GRCh38 carries a minor allele, where eight exons
361 encoding tandem repeat protein domain in *CR1* are inserted with respect to T2T-CHM13. In
362 addition, *ZDHHC11* (Zinc Finger DHHC-Type Containing 11) and *ZDHHC11B* are involved
363 in innate immune or anti-virus response by enabling signaling adaptor activity. The CNV of
364 *ZDHHC11* and *ZDHHC11B* are associated with hepatoblastoma⁵³ and primary open-angle
365 glaucoma⁵⁴. The *GSTM1* (glutathione S-transferase mu) locus is also a polymorphic locus
366 associated with cancers, metabolism, and hepatic cirrhosis⁵⁵. Thus, our study provides a
367 fundamental resource for functional assessments to examine functional differentiation
368 between/among polymorphic loci in humans. Importantly, it is still unclear whether the
369 reference bias has effects on the reported disease association study of these discrepant
370 regions. If so, the excess of the co-localization between the discrepant regions and disease
371 relevant CNV needs to be re-assessed.

372

373 We comprehensively compare the *KLRC* gene cluster in humans and NHPs. Firstly, we
374 precisely characterize the breakpoints of duplication and deletion of *KLRC2*. The breakpoints
375 on single-base-pair resolution could facilitate the molecular probe development to genotype
376 the CN of *KLRC2* in the future. The duplication and deletion mechanism of *KLRC2* are
377 associated with the *Alu* elements and simple repeats in the human genome. Notably, our
378 *KLRC* haplotype inference and phylogenetic tree analyses show that the origin of *KLRC2* and

379 *KLRC3* is duplicated from the common ancestor of the apes and Old World monkey. The
380 human population genetic analyses reveal that *KLRC*-hap2 (*KLRC2* depletion) is caused by a
381 single deletion event in humans. Africans and Asians have a higher frequency of *KLRC*-hap2
382 but we did not observe significant pi diversity change in the *KLRC* gene cluster in humans.
383 These results would suggest that the distribution of the *KLRC* haplotypes may simply be the
384 result of genetic drift in human evolution. Yet, we identified the six SNVs to distinguish
385 *KLRC*-hap2 (*KLRC2* depletion) from *KLRC*-hap1. The eQTL and GWAS analyses show the
386 gene expression and immune functional differentiation between the two *KLRC* haplotypes,
387 and previous functional experiments shows the *KLRC2* haplotypes have different roles in
388 synaptic pruning³⁵. Additional experiments are required to determine if loss of *KLRC2* is the
389 result of genetic drift or subject to other models of selection (e.g., balancing selection).

390

391 Our tests of selection implicate three amino acids of *KLRC3* as potentially subject to positive
392 selection during primate evolution. Predicted protein structures further suggest structural
393 differences (KLRCX/HLA-E/CD94) between KLRC2 (KLRC2/HLA-E/CD94) and KLRC3
394 (KLRC3/HLA-E/CD94). It is possible that *KLRC3* has acquired distinct functional properties
395 from *KLRC2* as a result of natural selection.

396

397 We also show that the *KLRC* gene cluster region was misassembled in GRCh38, likely
398 because the region was assembled by two BAC clones from two distinct *KLRC* haplotypes. If
399 we used the six SNVs to infer the *KLRC* haplotype, GRCh38 would carry *KLRC*-hap2
400 (*KLRC2* deletion). Yet, the GRCh38 shows *KLRC*-hap1 at present. As a result, association
401 studies of *KLRC* genes and their interpretation would be potentially confounded.

402

403 Altogether, our study provides a more comprehensive and detailed assessment of the
404 structure and function of the large-scale discrepant genomic regions between GRCh38 and
405 T2T-CHM13. We believe the results of this work not only contribute to our biological
406 understanding of these diverse regions but will benefit future studies by helping to eliminate
407 reference biases. We should stress that our study focused solely on the large-scale discrepant
408 regions between two ‘completed’ genome assemblies and, as such, represents a limited
409 survey of the true extent of human genome structural variation^{18,19}. It is anticipated that the
410 T2T Consortium will generate more complete genome assemblies from a diversity of human
411 samples and non-human primates. These will help us to fully understand the extent of

412 complex/discrepant regions in humans^{4-11,25,26} and their biological impact using reference-free
413 approaches.

414

415 **Methods**

416 **Data in this study**

417 We downloaded 94 long-read human genome assemblies from the HPRC phase 1 project
418 (<https://humanpangenome.org/>)²⁴⁻²⁶. We download the Illumina data of the 2,504 high-
419 coverage short-read from the 1KG human population dataset⁴³. For the reconstruction of the
420 phylogeny of the *KLRC* gene cluster, we locally assembled the *KLRC* gene cluster region
421 from the published HiFi reads of chimpanzee, bonobo, gorilla, orangutan, gibbon, macaque,
422 owl monkey, and marmoset. In addition, the ‘non-syntenic’ region, centromere, and gene
423 annotation files were downloaded from the UCSC Genome Browser directly
424 (<https://genome.ucsc.edu>). The (sub)telomere regions are defined as a 500 kbp region away
425 from the start or end of chromosome in this study.

426

427 **Discrepant region characterization and validation**

428 We used a reciprocal alignment approach to systematically characterize the SVs. In detail.
429 We used GRCh38 as the reference genome and T2T-CHM13 as the query to run PAV
430 (v2.0.0)^{18,19}, PBSV (PBSV, <https://github.com/PacificBiosciences/pbsv>, v2.8.0), and
431 minigraph²⁰ to characterize SVs. We also used T2T-CHM13 as the reference and GRCh38 as
432 the query to run PAV, PBSV, and minigraph to characterize SVs. Then, we LiftOver the
433 coordinates from GRCh38 to T2T-CHM13 and then merged these calls with bedtools
434 (v.0.29.0)⁵⁶. In the PBSV analysis, we used the PBSIM2 tool⁵⁷ to simulate HiFi reads from
435 GRCh38 and used these simulated reads against T2T-CHM13.

436

437 We developed a custom script to automatically screenshot the syntenic plots from Saffire
438 (<https://mr vollger.github.io/Saffire>). In addition, we integrated minimap2 (v2.24)²¹ or
439 mummer4 aligner²² to generate syntenic PAF files. We next applied the dotplot implement in
440 mummer4²² to generate dot plots. Then, we implement the above scripts into a website tool
441 (SynPlotter) to visualize the syntenic relationship between two coordinates. With our website
442 tool, the syntenic plot and dot plot can be generated, and the basic genomic difference
443 statistics could be calculated. The gene and repeat (e.g., segdups) annotations are also shown.

444 Lastly, we used our website tool to validate the large SVs (≥ 10 kbp) generated by the three
445 above callers.

446

447 **Gene, structural type, and repetitive sequence annotation for discrepant regions**

448 We used bedtools (v2.29.0)⁵⁶ to compare the discrepant regions between ‘non-syntenic’
449 regions and our large SVs (≥ 10 kbp). We used the ggplot2⁵⁸ and karyoploteR packages⁵⁹ to
450 plot the chromosome ideogram. Next, we characterized the discrepant regions into four types
451 (insertions, deletions, inversions, and SDRs) with eyes and manually refined the breakpoints
452 of these SVs.

453

454 We also used the gene, repetitive sequence annotation files from the UCSC Genome Browser
455 to annotate these discrepant regions with bedtools (v2.29.0)⁵⁶. In this study, the centromere
456 regions include pericentric regions, but not the centromeric transition regions in all analysis.
457 Notably, the previous study reported sequence difference between GRCh38 and CHM13, but
458 our study reported the location of the discrepant regions. In the Fig. 1, we counted the
459 number and the length of the discrepant regions as centromere (CEN), segdup (SD), telomere
460 (TEL), and tandem repeat (TRF) based on the location of them, not the absolute length of
461 sequences belonging to each type.

462

463 We used a hierarchy approach to define SV-location: (1). If a given SV located in CEN, we
464 counted it as CEN; (2). If a given SV located in TEL (500kbp from head or tail), we counted
465 it as TEL; (3). If a given SV located in segdup and includes at least 20% or 2kbp segdup
466 sequence, we counted it as SD; (4). If a given SV located in TRF and includes at least 10% or
467 1kbp sequence, we counted it as TRF; (5). If a given SV does not belong to any type of
468 above, we counted it as others. For example, if a given SV located in the centromere regions,
469 we counted it as CEN type no matter whether it contains segdup sequence or not.

470

471 **Structural polymorphism enrichment analysis**

472 To test whether the discrepant regions are more likely polymorphic, we downloaded the
473 SGDP CN table¹⁷ from the UCSC Genome Browser (<https://genome.ucsc.edu/>). Here, to
474 reduce the bias from the high CN (average CN estimation from SGDP ≥ 10 , n=53), we only
475 used the 131 discrepant regions (CN < 10) belonging to insertions, deletions, and SDRs to
476 calculate the standard deviations (s.d.) of the CN. First, we used bedtools (v.2.29.0)⁵⁶ to
477 intersect the 131 discrepant regions with the SGDP CN table and then calculated the s.d. of

478 the CN of each intersected region. Then, we calculated the mean and median values of
479 estimated s.d. (mean=0.735, median=0.439). These are our observed s.d. values of the 131
480 discrepant regions.

481

482 For null distribution, we did two experiments in this study. (1). Simulate the distribution of
483 mean s.d. of the whole genome. We used bedtools (v2.29.0)⁵⁶ to randomly shuffle the
484 corresponding number of coordinates (n=131) in the genomic regions where there are no
485 centromeres, telomeres, and CN<10. We intersected them with the SGDP CN table, and
486 calculated the s.d. of the CN for each intersected region. Then, we calculated the
487 mean/median s.d. value. (2). Simulate the distribution of mean s.d. of the CNV regions
488 (CN>2.5 and CN<10). We used bedtools (v2.29.0) to randomly shuffle the corresponding
489 number of coordinates (n=126) in the genomic regions where there are no centromeres,
490 telomeres, CN >2.5, and CN<10. We intersected them with the SGDP CN table, and
491 calculated the s.d. of the CN for each intersected region. Then, we calculated the
492 mean/median s.d. value.

493

494 We repeated this 1000 times for each experiment and calculated the empirical p-value of our
495 observed mean s.d. value (permutation test). In addition, we also estimated the observed
496 mean and median s.d. values of the SGDP CN table for the two experiments. (1). We
497 calculated the mean and median s.d. value of the regions (CN <10) based the SGDP CN table
498 (mean = 0.13, median =0.079). (2). We calculated the mean and median s.d. value of the
499 regions (CN <10 and CN >2.5) based on the SGDP CN table (mean = 0.58, median =0.463).

500

501 **Disease relevant CNV enrichment and survey**

502 We downloaded the CNV coordinates from the morbid and the cross-disorder dosage
503 sensitivity maps²⁸⁻³⁰ and LiftOver them to T2T-CHM13. We next used bedtools to intersect
504 our discrepant regions with the integrated coordinates and found 33 discrepant regions are co-
505 localized with the disease relevant CNVs. We also used a permutation test to shuffle the
506 discrepant regions in T2T-CHM13, excluding centromeres and telomeres, and calculated how
507 many discrepant regions could be co-localized with the disease relevant CNVs. We repeated
508 this process 1,000 times and plotted the distribution of the number of co-localized regions
509 (mean N=19.9) with ggplot2 in R.

510

511 We also manually curated the coordinates with gene annotations from the literatures and
512 DECIPHER database by hands. To better represent the disease relevant discrepant regions
513 (Table S5), we only listed the regions with well-qualified evidence/literature/case-report to
514 support as disease relevant in Table 1.

515

516 **Genomic syntenic comparison analysis**

517 In this study, we found 67 newly identified discrepant regions, of these, the 25 regions
518 contain 38 genes. Thus, we used minimiro (commit
519 18271297374ae6a679521a7ce3f5bb6c0cf8d261) to compare the genomic syntenic
520 relationships between GRCh38 and T2T-CHM13 in these regions.

521

522 Then, we used the RefSeq annotation from GRCh38 and CAT/RefSeq annotation from T2T-
523 CHM13 to extract the protein sequences of the genes. The mafft program (v7.4.3)⁶⁰ was used
524 to align the amino acid to check the amino acid difference among the homologous genes. The
525 schematic plots were generated by ggplot2 and AliView (v1.26)⁶¹.

526

527 ***KLRC2* haplotype characterization**

528 We extracted the genomic regions containing the *KLRC* gene cluster region from GRCh38
529 (chr12:10359648-10470462). Then, we used minimap2 (v2.24) to map the region to 94 long-
530 read human genome assemblies and other NHP long-read genome assemblies. Finally, we
531 used the minimiro to generate the syntenic plots between GRCh38 and other human and NHP
532 samples. We found three distinguished haplotypes of the *KLRC* gene cluster based on the CN
533 variation of *KLRC2*.

534

535 ***KLRC* haplotype inference from 1KG population dataset**

536 We used the previously reported read-mapping approach (SUNK-WSSD)^{39,40} to genotype the
537 CN of *KLRC2* and *KLRC3* in the 1KG population dataset (2,504 high-coverage Illumina
538 genomes). The mean CN of *KLRC3* of 2,504 humans is ~1.8 (s.d.: 0.14) (Fig. S4), while the
539 mean CN of *KLRC2* of 2,504 humans is ~1.9 (s.d.: 0.6). The CN of *KLRC3* is clustered
540 together in different human groups, suggesting there is no CN variation of *KLRC3* in humans
541 (Fig. S15). However, the CN of *KLRC2* is clustered into three groups in different human
542 groups, suggesting there is CN variation of *KLRC2* in humans.

543

544 If the CN of *KLRC2* is greater than 2.5 (mean + 1 s.d.), we inferred the *KLRC2* CN as 3. If
545 the CN of *KLRC2* is less than 1.3 (mean – 1 s.d.), we inferred the *KLRC2* CN as 1. Then, we
546 used the maps, ggplot2, and scatterpie packages
547 (<https://www.rdocumentation.org/packages/scatterpie/versions/0.1.8>) in the R to plot the
548 world map of the *KLRC* haplotype map.

549

550 **Phylogeny reconstruction and time-calibration tree reconstruction**

551 We used minimap2 (v2.4) to determine the syntenic regions in human and NHP genome
552 assemblies. We also used samtools (v1.9) to extract the corresponding regions. Then, we used
553 mafft (v7.453) to align the genomic sequence with default parameters and used it as input for
554 IQTREE (v1.6.11) to build the maximum likelihood phylogenetic trees^{21,62-64}.

555

556 To determine the time of duplication, we used BEAST2 (v2.6.2)⁶⁵ to date the phylogeny. The
557 prior calibrated times were used from the previous studies. Here, we used the log-normal and
558 the real mean model to set the prior calibrate time, including pan-lineage split time (~1.45
559 mya), owl monkey and marmoset split time (~24.5 mya), monkey and ape split time (~54
560 mya) in this study. The MCMC chains were run 30,000,000 steps and 3,000,000 steps were
561 set for burnin running. Finally, we used the tracer (v1.7.1) to examine whether the chain was
562 convergent. Indeed, each ESS value of each parameter was over 200 in our study and these
563 results suggested the MCMC chain was converged. FigTree (v1.4.4) and iTol
564 (<https://itol.embl.de/>) were used to plot the trees.

565

566 **Selection test with PAML and aBSREL**

567 We downloaded the human and NHP coding sequences (CDS) and protein sequences for
568 *KLRC2* and *KLRC3* from the UCSC Genome Browser. We used mafft (v7.4.3) to align the
569 protein sequences and used translatorx_vLocal.pl to align the CDS based on the aligned
570 protein sequences. All protocols are based on the previously reported tool (TREEEasy)⁶²⁻⁶⁴.

571

572 We examined the pi diversity of the *KLRC* gene cluster regions in humans with 94 long-read
573 genome genotyping data. Then, we ran a preliminary selection test on aBSREL⁴⁶
574 (<https://www.datamonkey.org/analyses>) and the aBSREL tool showed the selection signals
575 on the *KLRC3* clade. We also ran the branch model in PAML (v4.9)^{45,66} and the model
576 showed the selection signals on the *KLRC3* clade too (p=0.03). The branch-site model in
577 PAML (v4.9) shows three amino acids under selection with a probability greater than 0.9 in

578 the clade of KLRC3 in the Bayes Empirical Bayes (BEB) analysis (p=0.006). The p-values
579 were calculated by the likelihood ratio test in R.

580

581 **Protein structure analysis of KLRC2 and KLRC3**

582 We predicted the structural model of KLRC2 (residues 118-231) and KLRC3 (residues 118-
583 240) using AlphaFold2⁶⁷ and KLRC1 crystal structure^{33,47} with predicted local distance
584 difference test (pLDDT) values as 92.74 and 80.55, respectively, suggesting that they are
585 accurate enough for the further analysis. AlphaFold2⁶⁷ was used to predict the structures of
586 KLRC2/HLA-E/CD94 and KLRC3/HLA-E/CD94 complexes. The pLDDT values of the two
587 complexes are 80.39 and 76.05, respectively, which are of high confidences and are accurate
588 enough for the interaction analysis. Protein structure and interaction analyses were performed
589 on PyMol (v2.4.1, <https://pymol.org/>). Structure alignment shows obvious differences
590 between KLRC2 and KLRC3. Met223 of KLRC2 and Arg224, Arg227, and Gly229 of
591 KLRC3 are located at the surface loops which connecting two β -strands, and the loop of
592 KLRC3 has a longer conformation. His226 and Lys228 of KLRC2 may contribute to the
593 following β -strand, which is longer than that of KLRC3.

594

595 **eQTL analysis and GWAS ATLAS analysis**

596 We firstly aligned the *KLRC* gene cluster of 94 long-read human genome assemblies and we
597 used our custom script to find the SNVs that are different between *KLRC*-hap2 and *KLRC*-
598 hap1. Then, we investigated LD among Lewontin's D' and R2 implemented in
599 LDBlockShow (v1.40)⁶⁸ and PLINK (v1.90b6.21)⁶⁹ with 2,504 high-coverage genotyping
600 data from the 1KG dataset. The SNVs with minor allele frequencies >10% were used for this
601 analysis. We also calculated the allele frequency of the six distinguished SNVs in the
602 gnomAD dataset (v.3.1.2, <https://gnomad.broadinstitute.org/>)⁷⁰. The LD heatmaps were
603 generated by LDBlockShow or R.

604

605 We also used PLINK (v1.90b6.21)⁶⁹ to compute LD (measured with D') among all SNV
606 pairs. For each SNV pair, we then compared the reference alleles to the combinations of
607 alleles that were determined to be "in phase" (i.e., observed together on haplotypes more
608 often than expected under linkage equilibrium). For cases where the reference genome
609 carried alleles that were in phase, D' was retained as a positive value, whereas for cases
610 where the reference genome carried alleles that were out of phase, D' was multiplied by -1 to

611 indicate that the alleles are in repulsion. The same procedure was repeated for the
612 corresponding region of T2T-CHM13 as determined by LiftOver, using genotype data
613 produced by Aganezov et al⁶. For comparison, we also performed the same analysis for a
614 randomly selected “control” region of the same length (83.7 kbp) for both GRCh38 and T2T-
615 CHM13.

616

617 We downloaded the eQTL multi-tissue data from GTEx (release v8, <https://gtexportal.org/>)
618 and we extracted the gene expression associated with the six SNVs in different tissues. The
619 data showed that the six SNVs are only associated with *KLRC2* gene expression, as we
620 expected. Then, we used the ggplot2 package in R to plot the normalized effect size and p-
621 values of gene expression difference by the six SNVs. In addition, we also investigated
622 whether any locus is related to the reported genome-wide association study (GWAS). Then,
623 we download the phenome-wide association studies (PheWAS) data from GWAS ATLAS⁴⁴.
624 The data showed that three of the six SNVs are significantly associated with NK cells
625 (NKearly: %335+314- and NKeff: %314-R7-)³².

626

627 **Data availability**

628 The website tool SynPlotter is available at <https://synplotter.sjtu.edu.cn/>. The syntenic
629 comparison of discrepant regions is deposited in GitHub
(https://github.com/YafeiMaoLab/discrepant_region).

631

632 **Acknowledgements**

633 We thank T. Brown for assistance in editing this manuscript. We thank P. Hsieh and H.
634 Cheng for their comments and scripts. We thank the HPRC for providing the 94 long-read
635 human genome assemblies. The computations in this paper were run on the Siyuan-1 and π
636 2.0 cluster supported by the Center for High Performance Computing at Shanghai Jiao Tong
637 University.

638

639 **Funding**

640 This work was supported by Shanghai Pujiang Program (22PJ1407300) and Shanghai Jiao
641 Tong University 2030 Program (C-type) to Y.M.; and by National Natural Science
642 Foundation of China (82001372) to X.Y. This work was supported by Opening research fund
643 from Shanghai Key Laboratory of Stomatology, Shanghai Ninth People’s Hospital, College
644 of Stomatology, Shanghai Jiao Tong University School of Medicine (Grant No. 2022SKLS-

645 KFKT007) to Y.M. This work was supported, in part, by US National Institutes of Health
646 (NIH) grant# HG002385 to E.E.E. Additional funding included: NIGMS grants:
647 K99GM147352 (to G.A.L.) and National Natural Science Foundation of China grant:
648 32000812 (to J.S.). E.E.E. is an investigator of the Howard Hughes Medical Institute.
649

650 **Contributions**

651 Y.M. conceived the project. X.W., X.Y. and Y.M. finalized the manuscript. X.W., and Y.Z.
652 performed the SVs analysis. X.W., Y.Z., and X.Y. performed the analysis of large discrepant
653 regions. X.W., X.Y., and Y.M. performed the *KLRC* gene cluster analysis. M.X., Q.L., and
654 Y.M. performed the *KLRC* protein structure analysis. Y.M., D.J.T., R.C.M., and M.C.S.
655 performed the *KLRC2* haplotype swap analysis in GRCh38. S.Z. built the ‘SynPlotter’
656 website. Y.M., X.Y., X.W., M.X., M.R.V., N.C., W.T.H., G.A.L., D.M., J.S., R.C.M.,
657 M.C.S., W.L., Q.L., and E.E.E. contributed to interpret results and edited the draft
658 manuscript. All authors read, edited and approved the manuscript.
659

660 **Ethics declarations**

661 Conflict of interest
662 E.E.E. is a scientific advisory board (SAB) member of Variant Bio. N.C. is a full-time
663 employee of Exai Bio. The other authors declare that they have no conflict of interest.
664

665 **Reference**

- 666 1 Lander, E. S. *et al.* Initial sequencing and analysis of the human genome. *Nature* **409**
667 (2001).
- 668 2 Venter, J. C. *et al.* The sequence of the human genome. *Science* **291**, 1304-1351
669 (2001).
- 670 3 Navarro Gonzalez, J. *et al.* The UCSC genome browser database: 2021 update.
671 *Nucleic Acids Res.* **49**, D1046-D1057 (2021).
- 672 4 Nurk, S. *et al.* The complete sequence of a human genome. *Science* **376**, 44-53
673 (2022).
- 674 5 Altemose, N. *et al.* Complete genomic and epigenetic maps of human centromeres.
675 *Science* **376**, eabl4178 (2022).
- 676 6 Aganezov, S. *et al.* A complete reference genome improves analysis of human genetic
677 variation. *Science* **376**, eabl3533 (2022).
- 678 7 Gershman, A. *et al.* Epigenetic patterns in a complete human genome. *Science* **376**,
679 eabj5089 (2022).
- 680 8 Hoyt, S. J. *et al.* From telomere to telomere: The transcriptional and epigenetic state
681 of human repeat elements. *Science* **376**, eabk3112 (2022).
- 682 9 Vollger, M. R. *et al.* Segmental duplications and their variation in a complete human
683 genome. *Science* **376**, eabj6965 (2022).

684 10 Logsdon, G. A., Vollger, M. R. & Eichler, E. E. Long-read human genome
685 sequencing and its applications. *Nat. Rev. Genet.* **21**, 597-614 (2020).

686 11 Mao, Y. & Zhang, G. A complete, telomere-to-telomere human genome sequence
687 presents new opportunities for evolutionary genomics. *Nat. Methods* **19**, 635-638
688 (2022).

689 12 Eichler, E. E. Genetic variation, comparative genomics, and the diagnosis of disease.
690 *N. Engl. J. Med.* **381**, 64-74 (2019).

691 13 Fiddes, I. T. *et al.* Human-specific NOTCH2NL genes affect notch signaling and
692 cortical neurogenesis. *Cell* **173**, 1356-1369. e1322 (2018).

693 14 Suzuki, I. K. *et al.* Human-specific NOTCH2NL genes expand cortical neurogenesis
694 through delta/notch regulation. *Cell* **173**, 1370-1384. e1316 (2018).

695 15 Ishiura, H. *et al.* Noncoding CGG repeat expansions in neuronal intranuclear
696 inclusion disease, oculopharyngodistal myopathy and an overlapping disease. *Nat.*
697 *Genet.* **51**, 1222-1232 (2019).

698 16 Sone, J. *et al.* Long-read sequencing identifies GGC repeat expansions in
699 NOTCH2NLC associated with neuronal intranuclear inclusion disease. *Nat. Genet.*
700 **51**, 1215-1221 (2019).

701 17 Watkins, W. S. *et al.* The Simons Genome Diversity Project: a global analysis of
702 mobile element diversity. *Genome Biol. Evol.* **12**, 779-794 (2020).

703 18 Ebert, P. *et al.* Haplotype-resolved diverse human genomes and integrated analysis of
704 structural variation. *Science* **372**, eabf7117 (2021).

705 19 Porubsky, D. *et al.* Gaps and complex structurally variant loci in phased genome
706 assemblies. *bioRxiv* (2022).

707 20 Li, H., Feng, X. & Chu, C. The design and construction of reference pangenome
708 graphs with minigraph. *Genome Biol.* **21**, 1-19 (2020).

709 21 Li, H. Minimap2: pairwise alignment for nucleotide sequences. *Bioinformatics* **34**,
710 3094-3100 (2018).

711 22 Marçais, G. *et al.* MUMmer4: A fast and versatile genome alignment system. *PLoS*
712 *Comput. Biol.* **14**, e1005944 (2018).

713 23 Logsdon, G. A. *et al.* The structure, function and evolution of a complete human
714 chromosome 8. *Nature* **593**, 101-107 (2021).

715 24 Cann, H. M. *et al.* A human genome diversity cell line panel. *Science* **296**, 261-262
716 (2002).

717 25 Jarvis, E. D. *et al.* Semi-automated assembly of high-quality diploid human reference
718 genomes. *Nature* (2022).

719 26 Wang, T. *et al.* The Human Pangenome Project: a global resource to map genomic
720 diversity. *Nature* **604**, 437-446 (2022).

721 27 Dennis, M. Y. *et al.* The evolution and population diversity of human-specific
722 segmental duplications. *Nat. Ecol. Evol.* **1**, 1-10 (2017).

723 28 Cooper, G. M. *et al.* A copy number variation morbidity map of developmental delay.
724 *Nat. Genet.* **43**, 838-846 (2011).

725 29 Buttermore, E. *et al.* Neurodevelopmental copy-number variants: A roadmap to
726 improving outcomes by uniting patient advocates, researchers, and clinicians for
727 collective impact. *Am. J. Hum. Genet.* **109**, 1353-1365 (2022).

728 30 Collins, R. L. *et al.* A cross-disorder dosage sensitivity map of the human genome.
729 *Cell* **185**, 3041-3055.e3025 (2022).

730 31 Chen, J. *et al.* A pilot study on commonality and specificity of copy number variants
731 in schizophrenia and bipolar disorder. *Transl. Psychiatry* **6**, e824-e824 (2016).

732 32 Roederer, M. *et al.* The genetic architecture of the human immune system: a
733 bioresource for autoimmunity and disease pathogenesis. *Cell* **161**, 387-403 (2015).

734 33 Kaiser, B. K., Pizarro, J. C., Kerns, J. & Strong, R. K. Structural basis for
735 NKG2A/CD94 recognition of HLA-E. *Proc. Natl. Acad. Sci. USA* **105**, 6696-6701
736 (2008).

737 34 Vietzen, H. *et al.* Deletion of the NKG2C receptor encoding KLRC2 gene and HLA-
738 E variants are risk factors for severe COVID-19. *Genet. Med.* **23**, 963-967 (2021).

739 35 Marin, I. A. *et al.* The nonclassical MHC class I Qa-1 expressed in layer 6 neurons
740 regulates activity-dependent plasticity via microglial CD94/NKG2 in the cortex. *Proc.
741 Natl. Acad. Sci. USA* **119**, e2203965119 (2022).

742 36 Gigliotti, J. C. *et al.* GSTM1 Deletion Exaggerates Kidney Injury in Experimental
743 Mouse Models and Confers the Protective Effect of Cruciferous Vegetables in Mice
744 and Humans. *J. Am. Soc. Nephrol.* **31**, 102-116 (2020).

745 37 Dzikiewicz-Krawczyk, A. *et al.* ZDHHC11 and ZDHHC11B are critical novel
746 components of the oncogenic MYC-miR-150-MYB network in Burkitt lymphoma.
747 *Leukemia* **31**, 1470-1473 (2017).

748 38 Tschernoster, N. *et al.* Unraveling Structural Rearrangements of the CFH Gene
749 Cluster in Atypical Hemolytic Uremic Syndrome Patients Using Molecular Combing
750 and Long-Fragment Targeted Sequencing. *J. Mol. Diagn.* **24**, 619-631 (2022).

751 39 Mao, Y. *et al.* A high-quality bonobo genome refines the analysis of hominid
752 evolution. *Nature* **594**, 77-81 (2021).

753 40 Sudmant, P. H. *et al.* Diversity of human copy number variation and multicopy genes.
754 *Science* **330**, 641-646 (2010).

755 41 Sudmant, P. H. *et al.* Evolution and diversity of copy number variation in the great
756 ape lineage. *Genome Res.* **23**, 1373-1382 (2013).

757 42 Jiang, Z., Hubley, R., Smit, A. & Eichler, E. E. DupMasker: a tool for annotating
758 primate segmental duplications. *Genome Res.* **18**, 1362-1368 (2008).

759 43 McVean, G. A. *et al.* An integrated map of genetic variation from 1,092 human
760 genomes. *Nature* **491**, 56-65 (2012).

761 44 Watanabe, K. *et al.* A global overview of pleiotropy and genetic architecture in
762 complex traits. *Nat. Genet.* **51**, 1339-1348 (2019).

763 45 Yang, Z. PAML 4: phylogenetic analysis by maximum likelihood. *Mol. Biol. Evol.*
764 **24**, 1586-1591 (2007).

765 46 Smith, M. D. *et al.* Less is more: an adaptive branch-site random effects model for
766 efficient detection of episodic diversifying selection. *Mol. Biol. Evol.* **32**, 1342-1353
767 (2015).

768 47 Petrie, E. J. *et al.* CD94-NKG2A recognition of human leukocyte antigen (HLA)-E
769 bound to an HLA class I leader sequence. *J. Exp. Med.* **205**, 725-735, (2008).

770 48 Halldorsson, Bjarni V., et al. "The sequences of 150,119 genomes in the UK
771 Biobank." *Nature* **607.7920**, 732-740 (2022).

772 49 Noyes, Michelle D., et al. "Familial long-read sequencing increases yield of de novo
773 mutations." *The American Journal of Human Genetics* **109.4**, 631-646 (2022).

774 50 Porubsky, D. *et al.* Recurrent inversion polymorphisms in humans associate with
775 genetic instability and genomic disorders. *Cell* **185**, 1986-2005. e1926 (2022).

776 51 Brouwers, N. *et al.* Alzheimer risk associated with a copy number variation in the
777 complement receptor 1 increasing C3b/C4b binding sites. *Mol. Psychiatry* **17**, 223-
778 233 (2012).

779 52 Lambert, J.-C. *et al.* Genome-wide association study identifies variants at CLU and
780 CR1 associated with Alzheimer's disease. *Nat. Genet.* **41**, 1094-1099 (2009).

781 53 Wu, J.-F. *et al.* Copy-number variations in hepatoblastoma associate with unique
782 clinical features. *Hepatol. Int.* **7**, 208-214 (2013).

783 54 Lo Faro, V., Ten Brink, J. B., Snieder, H., Janssonius, N. M. & Bergen, A. A.
784 Genome-wide CNV investigation suggests a role for cadherin, Wnt, and p53
785 pathways in primary open-angle glaucoma. *BMC genomics* **22**, 1-20 (2021).
786 55 Gu, Y. *et al.* The influence of polymorphic GSTM1 gene on the increased
787 susceptibility of non-viral hepatic cirrhosis: evidence from observational studies. *Eur.*
788 *J. Med. Res.* **23**, 1-9 (2018).
789 56 Quinlan, A. R. & Hall, I. M. BEDTools: a flexible suite of utilities for comparing
790 genomic features. *Bioinformatics* **26**, 841-842 (2010).
791 57 Ono, Y., Asai, K. & Hamada, M. PBSIM2: a simulator for long-read sequencers with
792 a novel generative model of quality scores. *Bioinformatics* **37**, 589-595 (2021).
793 58 Ginestet, C. ggplot2: elegant graphics for data analysis. *J. R. Stat. Soc. Ser. A Stat.*
794 *Soc.* **174**, 245-245 (2011).
795 59 Gel, B. & Serra, E. karyoploteR: an R/Bioconductor package to plot customizable
796 genomes displaying arbitrary data. *Bioinformatics* **33**, 3088-3090 (2017).
797 60 Katoh, K., Misawa, K., Kuma, K. i. & Miyata, T. MAFFT: a novel method for rapid
798 multiple sequence alignment based on fast Fourier transform. *Nucleic Acids Res.* **30**,
799 3059-3066 (2002).
800 61 Larsson, A. AliView: a fast and lightweight alignment viewer and editor for large
801 datasets. *Bioinformatics* **30**, 3276-3278 (2014).
802 62 Li, H. *et al.* The sequence alignment/map format and SAMtools. *Bioinformatics* **25**,
803 2078-2079 (2009).
804 63 Nguyen, L.-T., Schmidt, H. A., Von Haeseler, A. & Minh, B. Q. IQ-TREE: a fast and
805 effective stochastic algorithm for estimating maximum-likelihood phylogenies. *Mol.*
806 *Biol. Evol.* **32**, 268-274 (2015).
807 64 Mao, Y., Hou, S., Shi, J. & Economou, E. P. TREEEasy: An automated workflow to
808 infer gene trees, species trees, and phylogenetic networks from multilocus data. *Mol.*
809 *Ecol. Resour.* **20** (2020).
810 65 Bouckaert, R. *et al.* BEAST 2: a software platform for Bayesian evolutionary
811 analysis. *PLoS Comput. Biol.* **10**, e1003537 (2014).
812 66 Yang, Z. PAML: a program package for phylogenetic analysis by maximum
813 likelihood. *Comput. Appl. Biosci.* **13**, 555-556 (1997).
814 67 Jumper, J. *et al.* Highly accurate protein structure prediction with AlphaFold. *Nature*
815 **596**, 583-589 (2021).
816 68 Dong, S.-S. *et al.* LDBlockShow: a fast and convenient tool for visualizing linkage
817 disequilibrium and haplotype blocks based on variant call format files. *Brief.*
818 *Bioinform.* **22** (2021).
819 69 Purcell, S. *et al.* PLINK: a tool set for whole-genome association and population-
820 based linkage analyses. *Am. J. Hum. Genet.* **81**, 559-575 (2007).
821 70 Collins, R. L. *et al.* A structural variation reference for medical and population
822 genetics. *Nature* **581**, 444-451 (2020).
823 71 Byman, E. *et al.* Alpha-amylase 1A copy number variants and the association with
824 memory performance and Alzheimer's dementia. *Alzheimers Res. Ther.* **12**, 158
825 (2020).
826 72 Davis, J. M., Heft, I., Scherer, S. W. & Sikela, J. M. A Third Linear Association
827 Between Olduvai (DUF1220) Copy Number and Severity of the Classic Symptoms of
828 Inherited Autism. *Am. J. Psychiatry* **176**, 643-650 (2019).
829 73 Wu, L. *et al.* Copy number variations of HLA-DRB5 is associated with systemic
830 lupus erythematosus risk in Chinese Han population. *Acta Biochim. Biophys. Sin.*
831 (*Shanghai*) **46**, 155-160 (2014).

832 74 Wu, Z. *et al.* Copy number variation of the Lipoprotein(a) (LPA) gene is associated
833 with coronary artery disease in a southern Han Chinese population. *Int. J. Clin. Exp.*
834 *Med.* **7**, 3669-3677 (2014).

835 75 Walker, L. C. *et al.* Evaluation of copy-number variants as modifiers of breast and
836 ovarian cancer risk for BRCA1 pathogenic variant carriers. *Eur. J. Hum. Genet.* **25**,
837 432-438 (2017).

838 76 Nelson, P. T., Fardo, D. W. & Katsumata, Y. The MUC6/AP2A2 Locus and Its
839 Relevance to Alzheimer's Disease: A Review. *J. Neuropathol. Exp. Neurol.* **79**, 568-
840 584 (2020).

841 77 Giannuzzi, G. *et al.* The Human-Specific BOLA2 Duplication Modifies Iron
842 Homeostasis and Anemia Predisposition in Chromosome 16p11.2 Autism Individuals.
843 *Am. J. Hum. Genet.* **105**, 947-958 (2019).

844 78 Mafra, F. *et al.* Copy number variation analysis reveals additional variants
845 contributing to endometriosis development. *J. Assist. Reprod. Genet.* **34**, 117-124
846 (2017).

847 79 Jin, X. *et al.* Copy Number Variation of Immune-Related Genes and Their
848 Association with Iodine in Adults with Autoimmune Thyroid Diseases. *Int. J.*
849 *Endocrinol.* **2018**, 1705478 (2018).

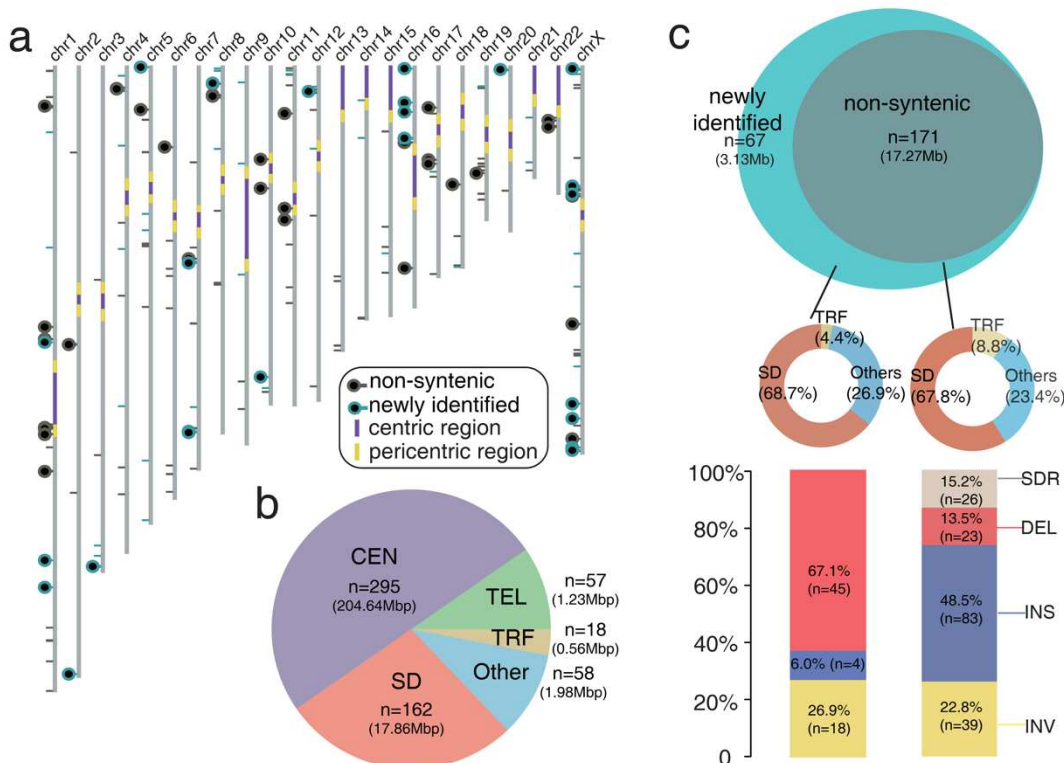
850 80 Grau, C. *et al.* Xp11.22 deletions encompassing CENPVL1, CENPVL2, MAGED1
851 and GSPT2 as a cause of syndromic X-linked intellectual disability. *PLoS One* **12**,
852 e0175962 (2017).

853 81 He, Y. *et al.* P2RY8 variants in lupus patients uncover a role for the receptor in
854 immunological tolerance. *J. Exp. Med.* **219** (2022).

855 82 Wen, M. *et al.* CT45A1 promotes the metastasis of osteosarcoma cells in vitro and in
856 vivo through β -catenin. *Cell Death Dis.* **12**, 650 (2021).

857 83 Yang, S. W. *et al.* A Cancer-Specific Ubiquitin Ligase Drives mRNA Alternative
858 Polyadenylation by Ubiquitinating the mRNA 3' End Processing Complex. *Mol. Cell*
859 **77**, 1206-1221.e1207 (2020).

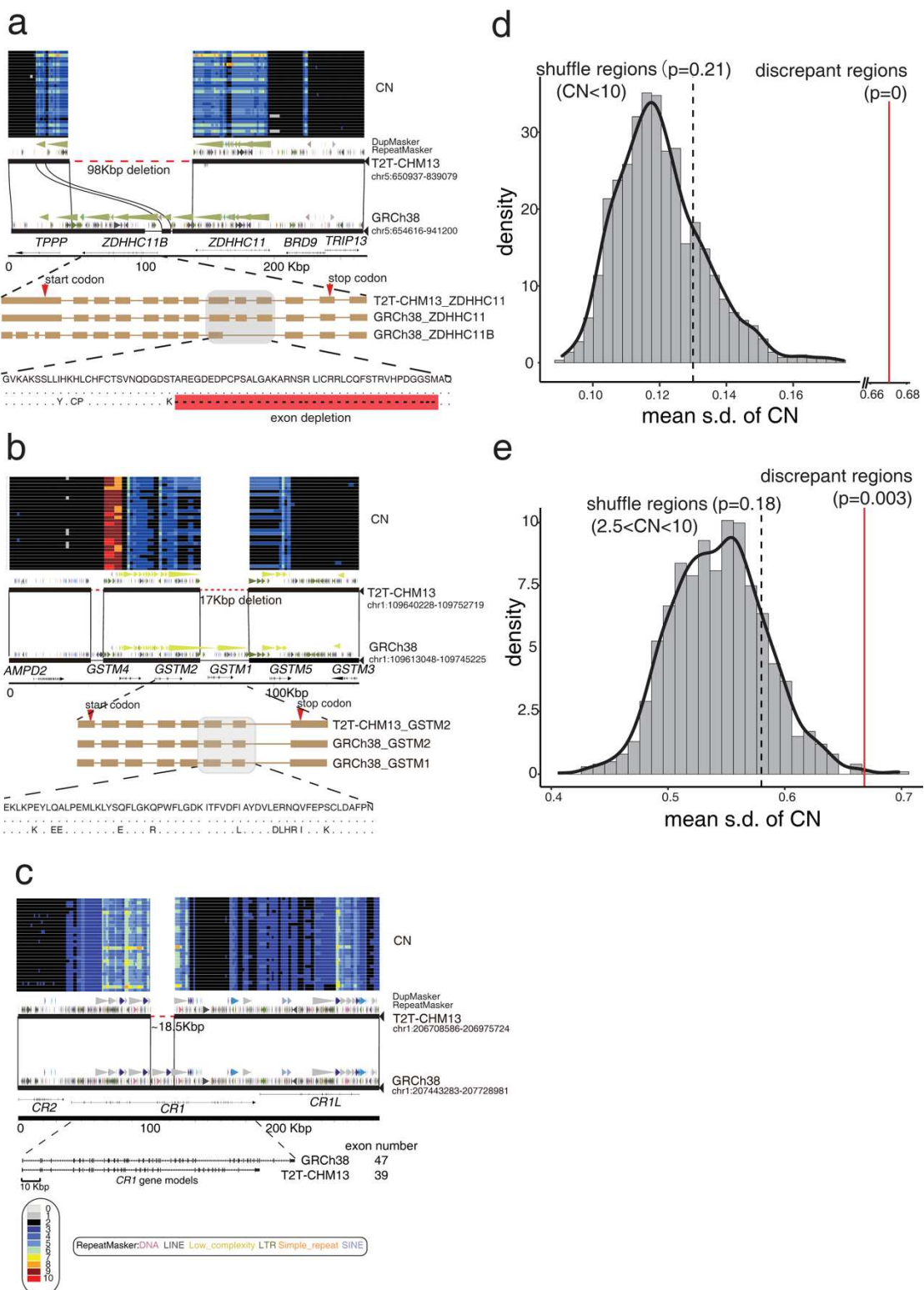
860 **Figure legends**



861

862 **Figure 1. The discrepant genomic regions between GRCh38 and T2T-CHM13. (a)**
863 Schematic of the T2T-CHM13 assembly depicts the centromere location (purple and yellow),
864 ‘non-syntenic’ region (black lines and circles), and newly identified discrepant region (cyan
865 lines and circles). Regions containing genes are represented with circles. (b) Pie chart of
866 genomic structure annotations of the 590 discrepant regions. The proportion of regions in
867 centromeres (CEN), telomeres (TEL), segdups (SD), tandem repeats (TRF), and others are
868 shown in light purple, green, dark red, yellow, and blue. (c) Venn diagram shows the
869 comparison of the discrepant regions between the previous studies^{4,9} and this study. The
870 genome structure annotations of ‘non-syntenic’ and newly identified regions are shown in the
871 middle panel. The components of structural variant types of ‘non-syntenic’ and newly
872 identified regions are shown in the bottom panel.

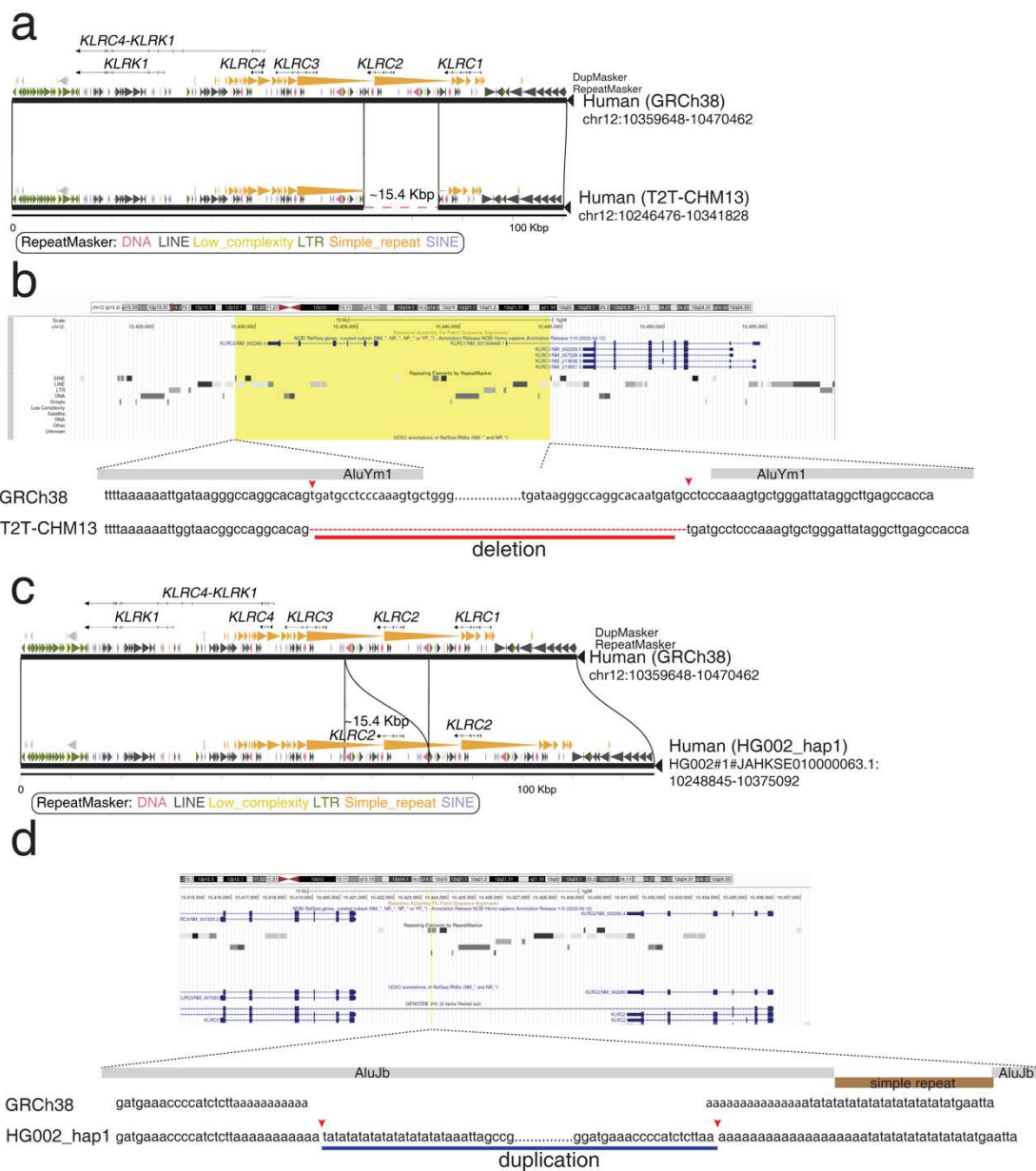
873



874

875 **Figure 2. Gene structure differences in the discrepant regions.** (a) The depletion of
 876 *ZDHHC11B* in the T2T-CHM13 genome assembly by a ~98 kbp deletion. The CN heatmap
 877 inferred from SGPD is shown in the top panel. The miropeat synteny relationship shows
 878 structural variation with repeat, duplication, and gene annotation. The exon schematic with
 879 amino acid alignment shows the gene model difference in the two assemblies. (b) The

880 depletion of *GSTM1* in the T2T-CHM13 genome assembly by a ~17 kbp deletion. (c) The
881 depletion of eight exons of *CR1* in T2T-CHM13 by ~18.5 kbp deletion. (d) The distribution
882 of the mean of s.d. of CN shows the mean s.d. of 131 discrepant regions (mean=0.735, red
883 line) is significantly higher than the simulated null distribution of s.d. of CN (CN<10,
884 empirical p=0). The black line represents the observed mean of s.d. of CN of the regions
885 where the CN is less than 10. (e) The distribution of the mean s.d. of CN shows the mean s.d.
886 of 131 discrepant regions (mean=0.735, red line) is significantly higher than the simulated
887 null distribution of s.d. of CN (2.5<CN<10, empirical p=0). The black line represents the
888 observed mean s.d. of CN of the regions where the CN is less than 10 and greater than 2.5.
889



890 duplication

891 **Figure 3. The syntenic comparison between different *KLRC* gene cluster haplotypes.** (a)

892 A ~15.4 kbp deletion in the T2T-CHM13 genome assembly results in the complete loss of

893 *KLRC2*. Gene structure, duplication, and repeat annotations are shown in the miropeat

894 diagram. (b) A screenshot of the *KLRC2* region from the UCSC Genome Browser is shown

895 in the top panel. The yellow box represents the ~15.4 kbp deleted sequence in the T2T-

896 CHM13 genome assembly. The nuclear sequencing alignment of the breakpoints is shown in

897 the bottom panel. Two Alu elements surrounding the breakpoints are shown in grey bars. (c)

898 A ~15.4 kbp duplication in the HG002_hap1 genome assembly results in the complete

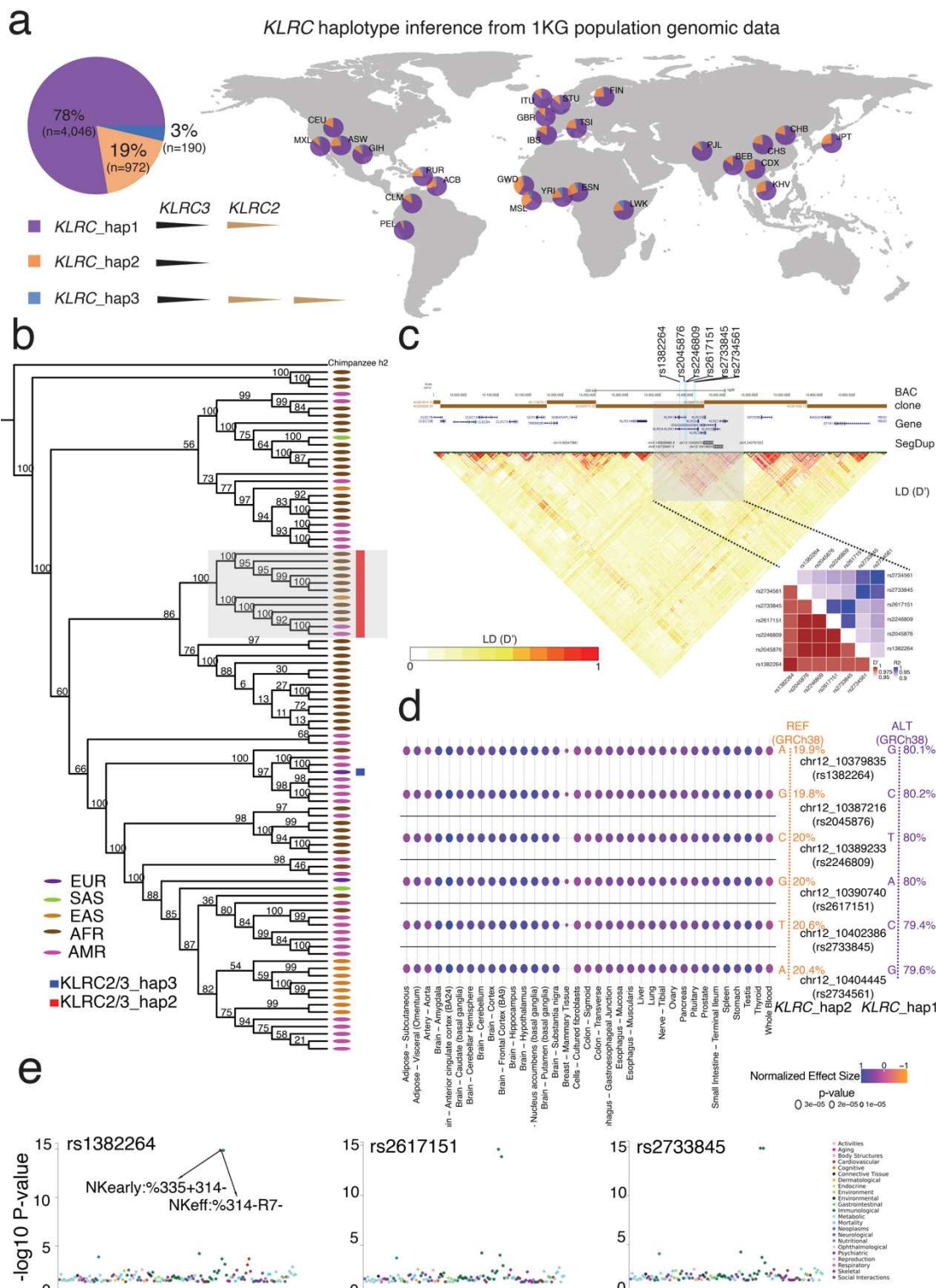
899 duplication of *KLRC2*. Gene structure, duplication, and repeat annotations are shown in the

900 miropeats diagram. (d) A screenshot of the *KLRC2* region from the UCSC Genome Browser

901 is shown in the top panel. The yellow line represents the position where the 15.4 kbp

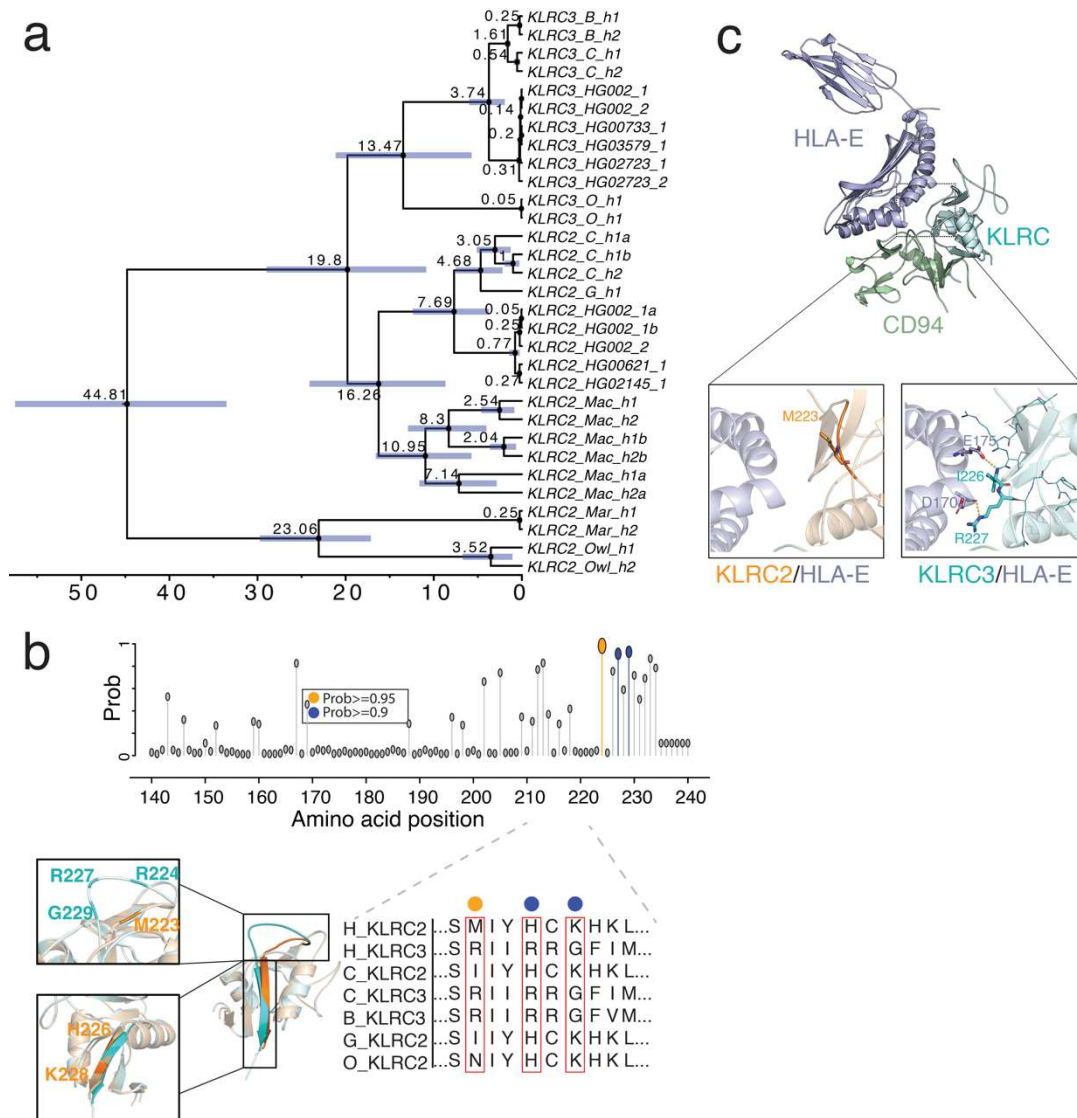
902 duplicated sequence is in the HG002_hap1 genome assembly. The nuclear sequencing
903 alignment of the breakpoints is shown in the bottom panel. The disrupted Alu element within
904 the breakpoints are shown in grey bars and a simple repeat disrupting the Alu element is
905 shown in a brown bar.

906



913 human population data across the world are shown on the right panel. (b) The phylogenetic
914 tree of the *KLRC* haplotype genomic regions shows *KLRC*-hap2 (*KLRC2* depletion) is a
915 result of a single deletion event. The red and blue rectangles show *KLRC*-hap2 and *KLRC*-
916 hap3, respectively. The rest of the humans belong to *KLRC*-hap1. The super population of
917 each human is listed with five color dots. (c) The genomic region (chr12:10,000,000-
918 10,700,000 in GRCh38) with assembled BAC clone, gene, segdup, and LD (D') annotation
919 shows that the *KLRC* gene cluster is probably linked together. The six SNVs distinguished
920 between *KLRC*-hap2 and *KLRC*-hap1 are represented in the cyan lines with their SNP ID.
921 The heatmaps of LD indexes (R2 and D') show that the six SNVs are highly linked in
922 humans. (d) Consistent patterns of associations between the six SNVs and expression levels
923 of *KLRC2* in 35 tissues are shown in the multi-tissue eQTL plots. The positive normalized
924 effect size (NES) values represent the effect of the higher expression on the alternative allele
925 (purple) relative to the reference allele (red). The (unadjusted) p values of the eQTL
926 association are shown in the size variable dots. The allele frequencies of the six SNVs in the
927 gnomAD database are shown on the right. (e) The PheWAS plots for three SNVs (rs1382264,
928 rs2617151, and rs2733845) are significantly associated with immune domain differentiation
929 across GWAS in the GWASALAS database. The particular traits (NKearly: %335+314- and
930 NKeff: %314-R7-) are marked with significant signals³².

931



932

933 **Figure 5. The potential functional differentiation between *KLRC2* and *KLRC3* by**
 934 **natural selection in primate evolution.** (a) The phylogenetic tree reconstructed from
 935 *KLRC2* and *KLRC3* of humans and other NHPs with BEAST2 shows the duplication of
 936 *KLRC2* and *KLRC3* occurred at the common ancestor of African great apes. The 95%
 937 confidence interval of the estimated age of each node is shown in the blue bar. All nodes are
 938 supported by one posterior possibility shown in dark circle dots. The texts: C, B, G, O, Mac,
 939 Mar, and Owl in the tips represent chimpanzee, bonobo, gorilla, orangutan, macaque,
 940 marmoset, and owl monkey, respectively. (b) The possibility of amino acid under positive
 941 selection inferred by the branch-site model in PAML is shown on the top panel. The grey,
 942 orange, and blue dots represent the possibility of less than 0.9, between 0.9 and 0.95, or
 943 greater than 0.95, respectively. The amino acid alignment of *KLRC2* and *KLRC3* among
 944 primates is shown on the bottom right panel. Structure alignment of predicted structures of
 945 *KLRC2* from residue 118 to 231 (orange, Uniprot: P26717) and *KLRC3* from residue 118 to

946 240 (cyan, Uniprot: Q07444). The zoomed-in pictures depict the structural discrepancies in
947 the loop (top) and the following β -sheet (bottom) between KLRC2 and KLRC3. (c) Predicted
948 structures of KLRC/HLA-E/CD94 complex (KLRC2 from residue 118 to 231: orange,
949 Uniprot: P26717; KLRC3 from residue 118 to 240: cyan, Uniprot: Q07444; Full-length
950 HLA-E: purple, Uniprot: I3RW89; CD94 from residue 57 to 179: green, Uniprot: Q13241).
951 The zoomed-in protein structure depicts the interaction interfaces of KLRC2/HLA-E (top)
952 and KLRC3/HLA-E (bottom).

953 **Table 1. The discrepant regions associated with human diseases**

Cytobands	CHM13_Position	Hg38_Position	Type	Reported CNV	Genes	Disease
1p13.3	chr1:109711485-109711489	chr1:109682999-109701443	DEL		<i>GSTM1</i>	Urinary system disease ³⁶
1p21.1	chr1:103546781-103735057	chr1:103697900-103697950	INV		<i>AMY1A, AMY1B, AMY1P1</i>	Neurological disease ⁷¹
1p36.13	chr1:16007445-16027869	chr1:16565700-16565800	INS		<i>NBPF1</i>	Neurodevelopmental disorders ⁷² , Cancer
1q21.1-1q21.2	chr1:143959965-143983984	chr1:146251047-148716074	INV		<i>BCL9, NOTCH2NLB, CHD1L, NBPF12, PRKAB2, FMO5, ACP6, GJA8, GPR89B, NBPF11, NBPF14, PPIAL4G</i>	Neurodevelopmental disorders ¹³⁻¹⁶
1q31.3	chr1:196105143-196105148	chr1:196758727-196843410	DEL		<i>CFHR3, CFHR1</i>	Immunological disease ³⁸
1q32.2	chr1:206810072-206810076	chr1:207542838-207561393	DEL		<i>CRI</i>	Neurological disease ^{51,52}
2q13	chr2:110517534-110698558	chr2:110095177-110276210	INV	Morbid CNV & Disease-related CNV	<i>NPHP1, MALL, MTLN</i>	Neurodevelopmental disorders ^{28,29} , Neurological disease ³⁰
3q29	chr3:198347865-198715835	chr3:195641035-195995576	DEL	Disease- related CNV	<i>MUC20, MUC4, TNK2</i>	Neurological disease ³⁰
5p15.33	chr5:684792-685093	chr5:686991-779053	DEL		<i>ZDHHC11B</i>	Cancer ³⁷
6p21.32	chr6:32339743-32356931	chr6:32486765-32530206	DEL		<i>HLA-DRB5</i>	Immunological disease ⁷³
6q26	chr6:161865491-161959834	chr6:160612509-160612509	INS		<i>LPA</i>	Cardiovascular disease ⁷⁴
7q35	chr7:145477647-145477649	chr7:144197172-144295737	DEL		<i>OR2A42, OR2A7, CTAGE8</i>	Cancer ⁷⁵
8p23.1	chr8:750030-11722000	chr8:8022351-12234558	INV	Morbid CNV	<i>DLGAP2, MYOM2, CLN8, ARHGEF, CSM1, MCPH1, ANGPT2, PRR23D1, DEFB103B, DEFB103A, DEF104A, DEF105A, XKR6, SOX7, TNKS, PPP1R3B, PPAG1, CTSB, ANGPT2, AGPAT5, ERI1, MSRA, DEFA5, FDFT1, GATA4, MFHAS1, PRSS5</i>	Developmental disorders ^{28,29}
10q11.22	chr10:48671598-48719249	chr10:47780140-47870155	SDR	Disease-related CNV	<i>GPRIN2</i>	Neurological disease ³¹
11p15.5	chr11:1076897-1087865	chr11:1017980-1017990	INS		<i>MUC6</i>	Neurological disease ⁷⁶
12p13.2	chr12:10315804-10315827	chr12:10429009-10444430	DEL		<i>KLRC2</i>	COVID-19 ³⁴ , Immunological disease ³²
16p11.2	chr16:30492288-30594258	chr16:30207700-30207750	INS	Disease- related CNV	<i>NPIP13, BOLA2B</i>	Neurological disease ^{30,77}
16p12.1-12.2	chr16:28619710-29091966	chr16:28339205-28811381	INV	Disease- related CNV	<i>SULT1A1, SULT1A2, NPIP8, NPIP6, EIF3CL, NPIP7, CLN3, IL27, EIF3C, NPIP9</i>	Neurological disease ³⁰
17p11.2	chr17:16716173-16767175	chr17:16813513-16821452	SDR	Disease-related CNV	<i>LGALS9C</i>	Neurological disease ³⁰
17q12	chr17:37341285-37441106	chr17:36393230-36459266	SDR	Disease-related CNV	<i>CCL3L1, CCL4L2, TBC1D3F</i>	Neurological disease ³⁰
19q13.2	chr19:42710594-42726422	chr19:39906200-39906250	INS		<i>FCGBP</i>	Reproductive system disease ⁷⁸

20p13	chr20:1629529-1629530	chr20:1580346-1613395	DEL		<i>SIRPB1</i>	Immunological disease ⁷⁹
22q11.23	chr22:24380000-24462473	chr22:23932712-24000827	SDR	Disease-related CNV	<i>GSTT2, GSTT4, DDT</i>	Neurological disease ³⁰
Xp11.22	chrX:50939534-50996879	chrX:51668108-51725222	INV		<i>CENPVL1, CENPVL2</i>	Neurodevelopmental disorders ⁸⁰
Xp22.33	chrX:1307333-1307498	chrX:1465426-1506104	DEL		<i>P2RY8</i>	Immunological disease ⁸¹
Xq26.3	chrX:134047172-134104452	chrX:13572163-3-135795043	SDR		<i>CT45A1, CT45A3, CT45A5</i>	Cancer ⁸²
Xq28	chrX:147946883-147987904	chrX:14968112-7-149722143	SDR		<i>MAGEA11</i>	Cancer ⁸³

954 Morbid CNV refers to the Ref. 28&29. Disease-related CNV refers to the Ref. 30.